Analog control of $La_{0.5}Sr_{0.5}FeO_{3-\delta}$ electrical properties through oxygen deficiency induced magnetic transition

Paul Nizet, Francesco Chiabrera, Nicolau López-Pintó, Nerea Alayo, Philipp Langner, Sergio Valencia, Arantxa Fraile Rodríguez, Federico Baiutti, Alevtina Smekhova, Alex Morata, Jordi Sort, Albert Tarancón**

Paul Nizet, Francesco Chiabrera, Nerea Alayo, Philipp Langner, Federico Baiutti, Alex Morata, Albert Tarancón
Department of Advanced Materials for Energy Applications, Catalonia Institute for Energy Research (IREC), Jardins de les Dones de Negre 1, 08930, Sant Adrià del Besòs, Barcelona, Spain
E-mail: fchiabrera@irec.cat , atarancon@irec.cat

Nicolau López-Pintó, Jordi Sort
Physics department, Universitat Autònoma de Barcelona, 08193 Cerdanyola del Vallès, Spain

Sergio Valencia, Alevtina Smekhova
Helmholtz-Zentrum Berlin für Materialien und Energie, Albert-Einstein-Str. 15, 12489 Berlin, Germany

Arantxa Fraile Rodríguez
Universitat de Barcelona, Departament de Física de la Matèria Condensada, Barcelona, 08028, Spain

Arantxa Fraile Rodríguez
Universitat de Barcelona, Institut de Nanociència i Nanotecnologia (IN2UB), 08028 Barcelona, Spain

Jordi Sort, Albert Tarancón
Catalan Institution for Research and Advanced Studies (ICREA), Passeig Lluís Companys 23, 08010, Barcelona, Spain

Switchability of materials properties by applying controlled stimuli such as voltage pulses is an emerging field of study with applicability in adaptive and programmable devices like neuromorphic transistors or non-emissive smart displays. One of the most exciting approaches to modulate materials performance is mobile ion/vacancy insertion for inducing changes in relevant electrical, optical, or magnetic properties, among others. Unveiling the interplay between changes in the concentration of mobile defects (like oxygen vacancies) and functional properties in relevant materials represents a step forward for underpinning the emerging oxide iontronics discipline. In this work, electrochemical oxide-ion solid-state pumping cells were fabricated for an analog control of the oxygen stoichiometry in thin films of mixed ionic-electronic conductor $La_{0.5}Sr_{0.5}FeO_{3-\delta}$. We demonstrate over more than 4 orders of magnitude electronic conductivity control at 50ºC within the same crystallographic phase through the precise and continuous voltage control of the oxygen stoichiometry. We show that behind the modification of the transport properties of the material lays a paramagnetic-to-antiferromagnetic transition. We exploit such magnetoelectric coupling to show control over the exchange interaction between $La_{0.5}Sr_{0.5}FeO_{3-\delta}$ and a ferromagnetic Co layer deposited on top.

1. Introduction

The tunability of specific material functional properties when exposed to different external conditions has drawn considerable attention in recent years. The external stimuli can be diverse, including temperature, pressure, incident light or electromagnetic fields.[1–3] More specifically, thin films of Transition Metal Oxides (TMOs) have shown to exhibit such a tunability with respect to heterogenous catalytic activity[4–6] as well as changes in the electronic structure,[7] in turn promoting the emergence of exciting phenomena such as high-temperature superconductivity, Colossal Magnetoresistance (CMR), or Metal-to-Insulator Transitions (MIT).[8–10] Modulation capabilities make thin film of TMOs potential materials for novel and advanced switchable devices such as neuromorphic transistors, memristors, and Resistive Random-Access Memories (Re-RAMs) that strongly depend on a precise tuning of the functional properties.[11–14]

An excellent example of the modulation of functional properties in TMOs can be found in the perovskite oxide $La_{1-x}Sr_xFeO_{3-\delta}$ (LSFx, x=0-1) family, a material system that finds multiple applications e.g. in Solid Oxide Fuel Cells (SOFC) electrodes,[15] catalyst for Oxygen Evolution Reaction (OER) [6,16] or as functional materials in advanced computing devices.[17] In the LSFx compounds, control of electronic, optical and catalytic properties can be achieved by two strategies: i) aliovalent Sr^{2+} substitution of trivalent La^{3+} (Sr'_{La} in Kroner-Vink notation), and ii) variation of oxygen deficiency δ. On the one hand, Sr substitution gives rise to a progressive increase of electron hole concentration, enabling a wide range of property change from an insulating and semi-transparent material for x=0 ($LaFeO_3$, LFO) to metallic and opaque for x=1 ($SrFeO_3$, SFO).[18] On the other hand, the introduction of oxygen deficiency tends to reestablish the insulating state, since the introduction of positively charged oxygen vacancies ($V_O^{\bullet\bullet}$) is naturally compensated by a reduction of electronic holes.[19] Engineering the functionalities of LSFx relies on controlling the acceptor dopant or the oxygen vacancy content. Notably, while the former is fixed during synthesis, the latter allows tunability during operation, potentially offering an analog control of the majority charge carrier concentration and the electronic properties.

However, depending on the Sr^{2+} substitution, different behaviors have been observed when reducing LSFx. For x>0.7, LSFx experiences a topotactic phase transition between the oxidized perovskite (PV) and the reduced Brownmillerite (BM) crystal structure, characterized by the formation of long-range oxygen vacancy ordering.[20,21] Electronic, optical and thermal conductivity varies substantially across this transition, with the BM phase of SFO (i.e. $SrFeO_{2.5}$)

presenting an insulating behavior similar to undoped LFO. [7,20–22] For x≤0.7, the BM transition is not usually reported, in contrast to other similar materials such as $La_{1-x}Sr_xCoO_{3-\delta}$ (LSC),[23] LSFx is expected to crystallize in perovskite structure with a random distribution of oxygen vacancies.[20,21] In this range, electronic transport properties as a function of the oxygen deficiency are not fully understood. Several studies carried out at high temperatures (T >500ºC) concluded that electronic conductivity varies almost linearly with electronic hole concentration (i.e. majority charge carriers).[24–26] This model, however, fails to predict the reported exponential variation of electronic conductivity with hole concentration in the intermediate-to-low temperature regime (T <500ºC).[18,19,27,28] The origin of the discrepancy between high and intermediate-to-low temperature conductivity measurements is still under debate. Some hypotheses suggest a blocking effect of the Fe-O-Fe conduction pathway induced by vacancy association mechanisms.[29] Density Functional Theory (DFT) calculations showed that oxygen vacancy might increase electronic hole localization [30] and its effective mass,[9] affecting the electronic transport. Understanding the effect of oxygen stoichiometry in PV LSFx may offer an advanced analog control of its functional properties (i.e., fine-tuning of properties within a wide, rather than discrete or binary, range of values) since, contrary to the BM/PV transition, oxygen ion concentration can be varied in a precise and continuous fashion.

Currently, the two main strategies to study functional properties as function of oxygen stoichiometry are pO_2 equilibration during deposition and annealing under controlled atmosphere.[7,23,31,32] Despite these techniques succeed in efficiently changing the oxidation state of thin film materials, they do not offer the precise control of the oxygen concentration. Moreover, temperature dependence studies are not possible since the oxygen equilibrium with the atmosphere, i.e., the final oxygen content in the material, shifts with temperature.[33] Recent studies have shown the possibility of using voltage gating through an electrolyte to modulate, in a reversible manner, the oxygen stoichiometry by fine tuning the oxygen chemical potential. Following this procedure, several studies have in-situ characterized the conductivity, magnetic and thermal properties of different oxides.[22,34,35]

In this work, we present a comprehensive study of the conductivity changes in $La_{0.5}Sr_{0.5}FeO_{3-\delta}$ (LSF50) as a function of oxygen deficiency and temperature (T= 50–350°C). A voltage-modulation approach is followed to enable reversible switching of oxygen stoichiometry in the LSF50 thin films while carrying out an in-situ characterization of the electronic functional properties. Sr-doping concentrations of x= 0.5 is studied to provide a broad understanding of the role of the oxygen defects preserving the PV structure, i.e. excluding the effect of

crystallographic phase transitions. To elucidate the origin of the changes in conductivity with oxygen vacancy concentration all along the range of conditions, electrical measurements are combined with optical (Spectroscopic Ellipsometry) and magnetic (Vibrating-Sample Magnetometry and Spin-resolved Photoemission-Electron Microscopy) characterization. According to a direct interrelation obtained between functional properties and defect concentration, the modulation of the electronic properties of LSF can be understood as a consequence of spin-order effects in these materials. We show that the voltage control of the oxygen stoichiometry in LSF50 can be used to manipulate the magnetic state of a cobalt ferromagnetic layer deposited on top, thus demonstrating the potential interest of LSF50 as an active material in magnetoionic field.

2. Results and Discussion

2.1. LSF50 conductivity modulation under applied voltage

The controlled modulation of electrical conductivity in LSF50 thin films was pursued by electrochemically pumping oxygen ions through an oxide-ion electrolyte. For this reason, an LSF50 thin film was deposited by Pulsed Laser Deposition (PLD) on 20 nm gadolinium-doped ceria (CGO)-coated Yttria Stabilized Zirconia (YSZ) (001) oxide ion-electrolytes (see Experimental Section for more details). Quality of the grown samples was checked via structural and surface characterization. The results revealed smooth layers of 100 nm in thickness and preferential out of plane (00l) orientation with a 45º in-plane rotation compared with the substrate fluorite unit cell (see Supplementary Material S1 and S2). **Figure 1a** shows a sketch of the configuration used to measure the electrical conductivity of a LSF50 layer during voltage-controlled oxygen ion insertion/extraction. The gating voltage (V_G) is applied across the YSZ substrate acting as an electrolyte. Four conductive stripes of 10 nm Ti/100 nm Au were microfabricated by lift-off and metal thermal evaporation to act as current collector and to perform 4-point contact conductivity measurements. Additionally, a capping layer of alumina (Al_2O_3) of approximately 100 nm was also deposited via PLD on top of the LSF50 thin film to prevent the equilibrium of the functional layer with the atmosphere. On the backside of the YSZ electrolyte, silver paste was painted to act as counter electrode (CE). The samples were then heated up till 350 ºC and an electrochemical potential was applied to the film with the CE grounded (V_G=-0.45 V to 0.1V). To ensure a proper stabilization of the material, the current flowing through the system (I_G) was measured (**Figure 1b** and Supplementary Material S3). Due to the pure oxide-ion conducting properties of YSZ substrates, this current represents the oxygen ions flowing from the CE, where oxygen incorporation/evolution is promoted by the

silver paste, to the LSF50 layer. As seen in Figure 1b, after each voltage step, I_G current goes to zero, indicating that the oxygen ion flow is correctly blocked by the alumina capping layer and electrochemical equilibrium at that specific potential is achieved.

The electrical conductivity (σ) of the LSF50 for different equilibrium states was then characterized in a two-steps process consisting of: (1) state setting by application of an electrochemical potential at 350 ºC (V_G=-0.45 V to 0.1V) and (2) temperature-dependent 4-point contact conductivity measurements (T=50-350 ºC) under open circuit voltage (OCV) conditions (I_G=0, see inset of **Figure 1c**). The two-steps process was repeated for all the different gate voltages (V_G=-0.45 V to 0.1V). Importantly, the non-volatility of the electrochemical state and the reproducibility of the measurements was assessed by measuring a constant conductivity and OCV after repeated cycles of V_G, temperature, and time (see Supplementary Material S3). Figure 1c shows the equilibrium conductivity presented as a function of V_G applied at different temperatures. Precise modulation of the conductivity with the voltage was achieved over more than four orders of magnitude in the whole range of temperatures, e.g. $\sigma=3\cdot10^{-3}$ S/cm at -0.4 V to $\sigma=1\cdot10^{2}$ S/cm at 0V when cooling down to T=50ºC after the state setting. As can be seen, the material presents a continuous increase in conductivity starting at negative potentials until reaching a plateau when approaching V_G= 0V. The next sections are dedicated to elucidating the effect of ion insertion into the LSF50 material.

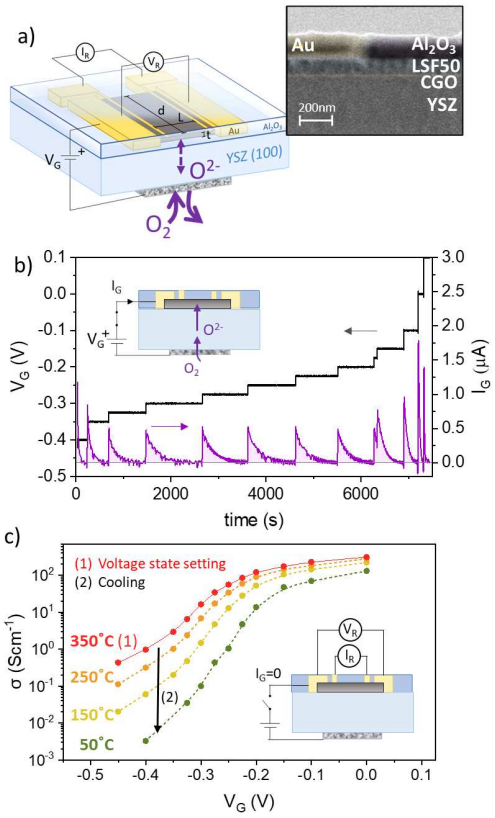

Figure 1. a) Sketch of the sample showing the main dimensions: thickness (t), width (d) and distance between pads (L); and the four-probe configuration for in-plane measurement of the electrical resistance and out-of-plane electrochemical pumping cell (Au/YSZ/Ag) for oxygen ion insertion in the LSF50 film. Purple arrows indicate the (de)insertion path of O into the film. The inset illustrates a cross-section SEM view of the sample including the alumina capping. b) Current stabilization of the LSF50 sample after the application of different gate voltages V_G. c) Conductivity measurements of the LSF50 layer after application of different V_G applied at 350ºC and subsequent cooling to different temperatures.

2.2. Control of the defect concentration in LSF50 with the applied voltage

First, the quantification of the oxide-ion insertion into LSF50 as a function of the applied voltage was carried out. In this regard, the application of an electrochemical potential (ΔE) to an oxide thin film through an oxide-ion electrolyte gives rise to a variation of its oxygen chemical potential, analogous to a modification of the equilibrium oxygen partial pressure

($pO_{2,eq}$) through the Nerst potential.[36,37] This shift modifies the defect equilibrium in the thin film leading to an increase/decrease of its oxygen concentration, similarly to batteries.[38] In the case of LSF50 thin films, the equilibrium with oxygen is governed by the following defect chemistry equation:[36,37]

$$\frac{1}{2}O_2 + V_O^{\bullet\bullet} + 2Fe_{Fe}^{x} \leftrightarrow O_O^{x} + 2Fe_{Fe}^{\bullet} \quad (1)$$

where Fe_{Fe}^{x}, O_O^{x}, $V_O^{\bullet\bullet}$, and $Fe_{Fe}^{\bullet}$ denote the Fe^{3+}, oxygen ions, oxygen vacancies and Fe^{4+} holes species respectively, according to the Kroger-Vink notation. In this equation, the incorporated oxygen atoms occupy vacant oxygen sites and the iron species, present in the structure initially in the form of Fe^{3+}, undergo oxidation to Fe^{4+}. Iron oxidation states, such as Fe^{2+} and Fe^{5+}, can be neglected within the range of temperature and oxygen partial pressure of this study.[37,38] Indeed, it is worth mentioning that the generalized treatment of the electronic holes as $Fe_{Fe}^{\bullet}$ is already a simplification as holes localize in the form of polarons over the Fe-O bond.[18,27,30] Two electron holes are formed upon incorporation of a single oxygen atom, i.e. $[Sr_{La}']=2\delta+[Fe_{Fe}^{\bullet}]$. As a consequence, the change of oxygen stoichiometry induced when modifying oxygen equilibrium through V_G involves a current (I_G) flowing through the system (see Figure 1b). The integration of this current along the transition between stable states can be used to calculate the change in oxygen stoichiometry ($\Delta\delta$) in the material (see **Figure 2a**):[39]

$$\Delta\delta = -\frac{c_{LSF}^3}{2eV_{film}}\int_0^t I_G(t)dt \quad (2)$$

where c_{LSF} is the lattice parameter and V_{film} is the volume of the film. Considering that according to previous studies the samples were entirely reduced under the lowest $pO_{2,eq}$ (i.e. $[Sr_{La}']=2\delta$ and $[Fe_{Fe}^{\bullet}]=0$),[36,37] one can calculate the state of oxidation of the iron in the material and the oxygen content as a function of the applied voltage. This assumption and the obtained stoichiometry values were confirmed by employing in-situ ellipsometry using a methodology recently developed by the authors (see Supplementary Material S4).[36]

Figure 2b depicts the oxidation state of iron (and oxygen content 3- δ) in the LSF50 sample as a function of the $pO_{2,eq}$ (and V_G) at 350ºC. The material reaches a maximum non-stoichiometry of δ=0.25 and follows a sigmoidal-type shape behavior expected from the dilute model proposed by Mizusaki et al.[24] and described by Equation 1 (assuming non-interacting oxygen vacancies, see Supplementary Material S3). In the case of the experimental data, the fit of the oxidation curve with this model yields to an equilibrium oxidation constant of Equation 1 of K_{ox}=5000, which falls within the expected range.[24,36,37] The slight deviations from the fit when

approaching the maximum oxidation state are likely due to non-dilute interaction, as reported by Tang et al.[36] This good agreement with the defect chemistry model indicates that the oxygen content in LSF50 thin films follows the expected behavior of a single-phase solid solution system. Additionally, chemical capacitance measurements performed by EIS also showed good agreement with the observed trend of oxidation state as a function of V_G (see Supplementary Material S3). Moreover, a complete section in the Supplementary Material discusses the potential effect of the CGO interlayer and the Ti adhesion layer on the electrical measurements and current integration (see Supplementary Material S11). This is also confirmed by ex-situ X-Ray diffraction (XRD) analysis, which revealed that the structure expanded upon reduction but retaining its PV phase (see Supplementary Material S2). Notably, **Figure 2c** shows that the increase of lattice parameter is consistent with the variation of Fe-O bond length predicted by a simple hard sphere approximation as the smaller Fe^{4+} (58.5 pm) is substituted by the larger Fe^{3+} ions (64.5 pm).[40,41] The consistency with the lattice parameters measured in literature for fully oxidized LSFx with different Sr content suggests that the iron oxidation state presents the main influence on the lattice parameter of the PV phase.[42,43]

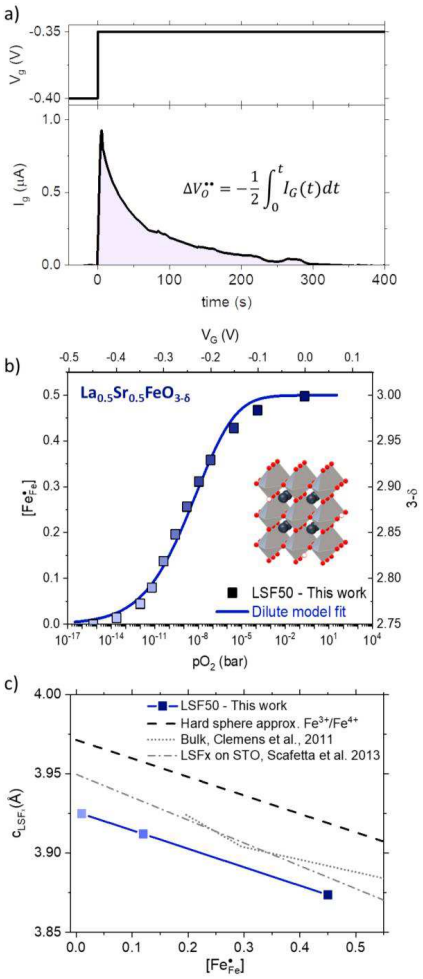

Figure 2. a) Exponential decay of the current after application of a voltage step. Its integration allows for the calculation of the charge and, consequently, the final oxidation state. b) Oxidation curve extracted from current integration for LSF50 at 350ºC. The figure also includes the relation between $[O_O^X]$ =3-δ and $[Fe_{Fe}^{\bullet}]$. The inset is a schematic of the PV structure, symbolizing the single-phase solid solution model employed for the fitting shown in blue line. c) Calculated cell parameter from ex-situ XRD of the LSF50 samples after the application of different V_G at 350ºC indicated by the calculated $[Fe_{Fe}^{\bullet}]$. Reference measurements on LSFx cell parameters are also shown for comparison in grey dotted and dash-dotted lines.[42,43]

2.3. The effect of oxygen deficiency on the electrical and optical conductivity

To understand the origin of the changes in the electronic transport of LSF50, the conductivity of the layers was measured as a function of the concentration of charge carriers ($Fe_{Fe}^{\bullet}$) at constant temperature in the range of T=50-350ºC (see **Figure 3**). Importantly, this analysis is possible because of the battery-like configuration of our system and the Al_2O_3 capping layer, which ensures that under OCV (I_G=0) the sample does not equilibrate with the atmosphere and retains its defect concentration upon time and temperature cycling (see Supplementary Material S3). The evolution of electrical conductivity shown in **Figure 3a** appears to change exponentially with the hole concentration $[Fe_{Fe}^{\bullet}]$ and cannot be simply explained by the variation of the charge carriers. Moreover, decreasing the temperature is observed to affect the conductivity of oxygen deficient LSF50 more than the oxidized one, suggesting an intricate behavior between charge carrier and mobility.

To investigate this point, conductivity results are displayed in an Arrhenius-like representation for different $[Fe_{Fe}^{\bullet}]$, see **Figure 3b**. The conductivity exhibits a linear relationship in ln(σT) vs 1/T for the most reduced states and oxidized states suggesting that the electronic transport in the thin film can be characterized by adiabatic small polaron hopping conduction. Electronic conductivity of LSF is commonly described by the polaron hopping model where the holes, localized over the Fe-O bond, can move to the Nearest Neighbor Hopping site with the assistance of phonons, [18,28,33] i.e. showing a thermal activation that follows an Arrhenius law with a certain activation energy (E_a) and pre-exponential factor (σ_o):[44,45]

$$\sigma(T) = \frac{\sigma_o}{T} exp\left(\frac{E_a}{k_b T}\right),\ \sigma_o = \frac{e^2 \nu}{a k_b}[Fe_{Fe}^{\bullet}] \cdot [Fe_{Fe}^{x}] \qquad (3,4)$$

where e, ν, a are the electron charge, the polaron attempt frequency and the site-to-site hopping distance, respectively. The preexponential factor in this model is the isothermal conductivity term of the equation and includes the probability of finding an $Fe_{Fe}^{\bullet}$ next to an Fe_{Fe}^{x} site. Although the conductivity can be described with the polaron model for the most reduced and oxidized states, there is a change in the slope between the reduced and oxidized states of LSF50, strongly suggesting a close relationship between the activation energy and the hole concentration. The trend was equally followed with the non-adiabatic polaron hopping model leading to the same analysis outputs (see Supplementary Material S5). To analyze this change, **Figure 3c and 3d** illustrate the variation in E_a and σ_o as a function of the hole concentration fitted over different temperature ranges. The activation energy starts from a constant value of 0.35 eV for the fully reduced material and then progressively decreases to a value of 0.1 eV as

the material oxidizes. This decrease does not happen simultaneously for all the temperatures, but there is a strong temperature dependance on the precise $[Fe_{Fe}^{\bullet}]$ values at which this E_a decrease occurs. Actually, when examining a specific oxidation state, the E_a diminishes as the temperature increases. A clear illustration of this transition can be seen at $[Fe_{Fe}^{\bullet}]$=0.25, where the activation energy is 0.35 eV at low temperatures and gradually decreases, reaching 0.15 eV at 325 °C. A non-trivial behavior in the σ_o evolution in Figure 3d is also seen. At the highest measured temperatures, small variations in the preexponential factors are seen. Nevertheless, low temperature σ_o plots show an exponential increase with $[Fe_{Fe}^{\bullet}]$. This exponential evolution of σ_o is followed up to a given $[Fe_{Fe}^{\bullet}]$ in which it suddenly decreases back to values close to 10^6 S·K·cm^{-1}. The exact $[Fe_{Fe}^{\bullet}]$ at which the maximum of σ_o is observed matches well with the onset of the decrease of E_a. This suggests a relation between the high activation energy states (E_a= 0.35 eV) and the exponential increase of σ_o with $[Fe_{Fe}^{\bullet}]$ ($\sigma_o \; \alpha \; e^{[Fe_{Fe}^{\bullet}]}$).

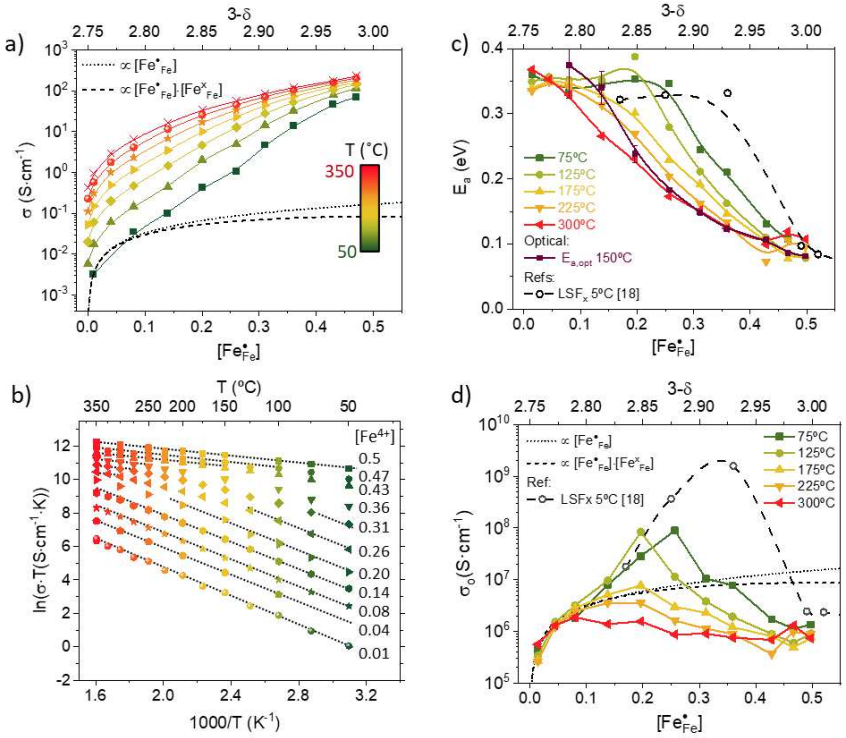

Figure 3. a) Conductivity of LSF50 as a function of the hole concentration for different temperatures. Solid line shows the expected change in conductivity according to the polaron hopping model. b) Arrhenius plot of the LSF50 conductivity at different oxidation states. The

numbers on the right indicate the $[Fe_{Fe}^{\bullet}]$. c-d) Activation energy (E_a) and preexponential factor (σ_o) dependance on the temperature and oxidation state extracted from the Arrhenius fitting of the conductivity. The dashed line corresponds to Xie et al. study.[18] $E_{a,opt}$ extracted from the optical measurements at 150C is also plotted.

Up until now, the results suggest a thermally activated transition, which remarkably lowers the activation energy for polaron hopping. The origin of this transition cannot be attributed to a phase change towards BM, as no structural transition was observed in the films (see Supplementary Material S2). Phase mixing models also failed to fit the LSF50 data (see Supplementary Material S8) as no mixture of a highly conductive and insulating regions is expected in this single-phase material.[46] Interestingly, a similar decrease of activation energy in the LSFx family had been documented in studies involving fully oxidized samples with varying Sr contents ranging from 0.17 to 1.[18,47] As a matter of comparison, the values extracted from the study of Xie et al.[18] as a function of Sr concentration (assuming a fully oxidized $[Sr_{Sr}'] = [Fe_{Fe}^{\bullet}]$ equilibrium) for a lower T range (5 ºC) are also plotted in **Figure 3c**. The evolution of the preexponential factor is also shown **Figure 3d**. The trend of both sets of data match for the most reduced and oxidized region, both for E_a and σ_o. However, the $[Fe_{Fe}^{\bullet}]$ at which the E_a starts to decrease and σ_o presents its maximum is higher in the study of Xie et al. compared to our data, which delineates a trend with the T-range investigated (see values extracted at lower T in Supplementary Material S6). The comparison suggests that the conductivity is mainly dependent on the hole concentration $[Fe_{Fe}^{\bullet}]$ and on the T range, regardless if modified by the aliovalent doping concentration or the oxygen deficiency, therefore excluding strong interaction between holes and other point defects ($V_O^{\bullet\bullet}$ or Sr_{La}') or other mechanisms of oxygen vacancies ordering.

Previous studies have correlated the hole concentration in LSFx to modifications of its band structure, which could explain the transition from a conductive to insulating state.[18,27,30] To find a direct correlation with the electrical transition, in-situ spectroscopic ellipsometry measurements were carried out as a function of the oxidation state and temperature (see Experimental and Supplementary Material S4). **Figure 4a** displays the optical conductivity for different $[Fe_{Fe}^{\bullet}]$ at a fixed temperature of 350°C. Starting with the most reduced state and progressing towards the more oxidized ones, an increase in the intensity and a red shift of the infrared (A) and visible (B) transitions at the expense of UV transition (C) is observed (see Supplementary Material S7 for a more detailed description on the band structure evolution of the LSFx family of materials). This progressive evolution of the band structure is visible in the decrease of the onset energy of transitions A and B upon oxidation (**Figure 4b**), calculated by

direct-forbidden Tauc-plots (see Figure S8 in Supplementary Material). The trend observed for transition B well matches with the literature data of oxidized LSFx thin films with different Sr content when plotted as a function of $[Fe_{Fe}^{\bullet}]$, confirming that electronic holes are the main responsible for band structure modification.[27] Although this band-closing goes in line with the increase of electronic conduction, we note that the optical bandgap of B is not affected by temperature, in disagreement with what observed for the onset of the electronic transition, see Figure 3. On the contrary, the bandgap of A presents a clear variation with temperature.

To gain further insights into this behavior, **Figure 4c** reports the deconvoluted optical conductivity of transition A measured for three different $[Fe_{Fe}^{\bullet}]$ as a function of T (see Supplementary Material S4 for details on the deconvolution). In the most oxidized case, $[Fe_{Fe}^{\bullet}]$= 0.5, the shape and position of the peak barely change, while for intermediate states ($[Fe_{Fe}^{\bullet}]$= 0.26 and $[Fe_{Fe}^{\bullet}]$= 0.2) a progressive red shift of the peak energy is observed as the T is increased, in agreement with the behavior measured for E_a. As the results suggest a relation between the polaron hopping energy and transition A, we tested this hypothesis in the frame of the optical adiabatic small polaron model developed by Holstein.[45] According to this theory, transition A is related to the photon energy ($h\omega_p$) required to induce polaron excitation from one Fe-site to its adjacent counterpart, following the equation $h\omega_p = 2E_p$, where E_p is the polaron formation energy.[48,49] Considering the adiabatic approximation, the relation between polaron hopping energy and E_p becomes:[45]

$$E_{a,opt} = \frac{1}{2}E_p - J = \frac{1}{4}h\omega_p - J \qquad (5)$$

wherein J represents the transfer energy, typically hovering around 0.1 eV.[49] Together with the experimental E_a obtained for electrical measurements, Figure 3c includes the activation energy extracted from the optical measurements considering J = 0.1 eV (see more details in Supplementary Material S4). The evolution of $E_{a,opt}$ closely follows the electrical E_a, revealing the polaron hopping nature of transition A. The good agreement between optical and electrical measurements shows that the evolution of polaronic characteristics can be tracked by optical conductivity.

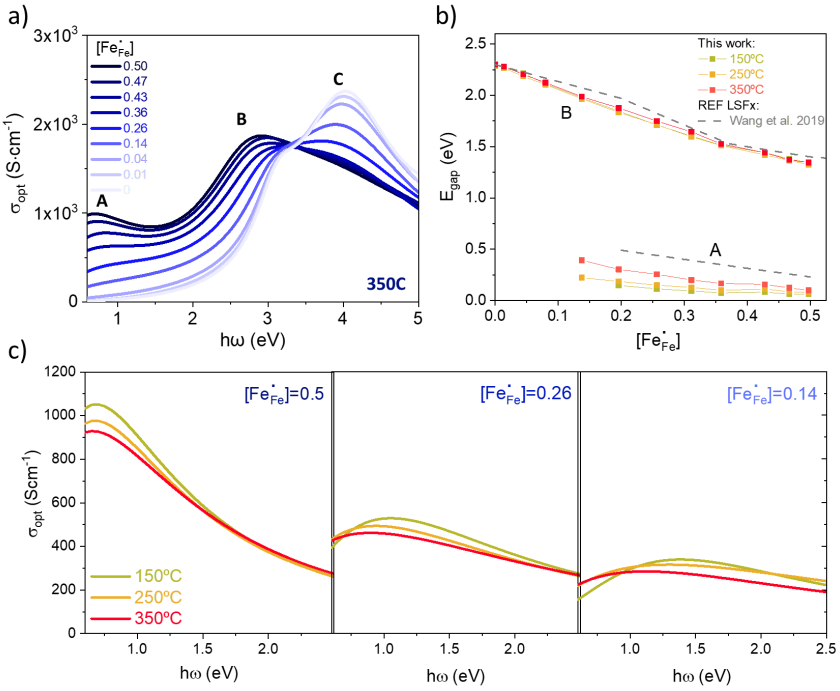

Figure 4. a) Calculated optical conductivity for the different measured oxidation states indicated by their $[Fe^{4+}]$ at 350C for LSF50. b) Calculated band gap closing as a function of $[Fe^{4+}]$. The figure also includes the band evolution of different fully oxidized LSFx from Wang et al.[27] c) Optical conductivity of the first transition peak at three different oxidation states indicated by the $[Fe^{4+}]$ measured at different temperatures.

Overall, the optical analysis reveals that the evolution of the band-structure upon oxygen variation, represented by the onset of B, cannot account for the thermal behavior observed in the electrical behavior. Transition A is instead able to properly reproduce the electrical transition, which can be explained in the frame of the optical adiabatic small polaron model. Therefore, combined optical and electrical measurements show that, for a constant electronic hole concentration, the activation energy tends to decrease while increasing the temperature, highlighting the thermal sensitivity of the transition. In this regard, electron transport in oxides, along with other properties, is very sensitive to the type of interaction between B-site cations through oxygen atoms.[9,50–52] Given the spin-order relation to these exchange interactions, the magnetic properties of LSF50 were also investigated.

2.5. The impact of magnetic properties on the electronic conductivity of LSF50

Considering the parent compound $LaFeO_3$, a super-exchange (SE) interaction between neighboring Fe^{3+} results in the establishment of an antiferromagnetic (AFM) interaction, characterized by a Néel Temperature (T_N) of 430 ºC.[53,54] From Goodenough-Kanamori rules it is expected that a mixed Fe^{3+}/Fe^{4+} valence promotes instead the ferromagnetic (FM) spin alignment through double-exchange (DE) interactions, resulting in FM or paramagnetic state (PM) for aliovalent Sr substitution.[51–53,55] Within the LSFx family, the second case typically prevails and so, in this scenario, fully oxidized LSF50 is paramagnetic. The reduction of the oxygen content is expected to promote an AFM phase similar to that of $LaFeO_3$, with an antiferromagnetic axis lying in-plane, parallel to the crystallographic *a*-axis.[54,56]

The magnetic domain state of two 100 nm-LSF50 layers, one previously reduced and the other previously oxidized electrochemically at 350ºC and quenched to room temperature, has been imaged by means of X-ray photoemission-electron microscopy (PEEM) using X-ray magnetic linear dichroism (XMLD) as magnetic contrast mechanism. XMLD is proportional to the square of the magnetic moment and hence commonly used for the investigation of AFM compounds.[57–59] Since no alumina capping could be used due to the low probing depth of XAS, the oxidation state of the samples was measured ex-situ by ellipsometry ($[Fe_{Fe}^{\bullet}]$= 0.04 and 0.5 for the reduced and oxidized, respectively). **Figure 5a and 5b** show the XMLD images obtained at the Fe L_2 edge, see Experimental section, for the reduced and oxidized samples, respectively. A clear pattern arising from the AFM domains is observed for the reduced sample. The AFM domain size in the reduced LSF50 is in good agreement with the previously documented in $LaFeO_3$ corroborating the role of SE interaction in AFM order in the LSF family of materials.[57–59] On the contrary, no domains were detected within the oxidized region irrespective of the angle of the incoming linearly polarized radiation with respect to the samples surface. In agreement with a paramagnetic phase, no domains could be seen as no linear dichroism is observed in the XMLD when surpassing the Neel temperature.

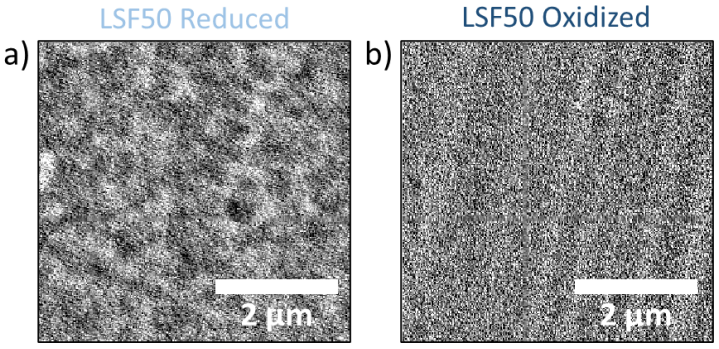

Figure 5 XMLD-PEEM images of antiferromagnetic domain patterns recorded for the reduced **(a)** and oxidized **(b)** LSF50 samples.

Having assessed the antiferromagnetic/paramagnetic (AFM/PM) transition in LSF50 thin films upon oxidation, we further explored the relation between magnetic and electrical properties. First, the T_N was obtained from the temperature dependence of the magnetization (M) for different oxidation states ($[Fe_{Fe}^{\bullet}]$ =0.1, 0.3, 0.46). The measurements were performed at a constant field (H=1kOe) as shown in Figure S16 in Supplementary Material. A change in the M curve was observed in all oxidation states that was assigned to the AFM/PM transition. The T_N of the sample was determined as a function of $[Fe_{Fe}^{\bullet}]$ (see Figure S16 in Supplementary Material). **Figure 6a** shows the T_N values extracted from the measurements. Although the precision is not high due to the wide temperature span of the transition, the results show good agreement with bulk measurement of T_N carried out by Wattiaux et al.[53] as a function of $[Fe_{Fe}^{\bullet}]$, also presented in Figure 6a. The temperature-span of the electrical transition was also derived from Figure 3c, considering the temperatures at which the E_a sets at its resistive state ($T_{Ea,set}$) and at its conductive state ($T_{Ea,On}$) (see Supplementary Material S6 for the procedure). Their values are included in Figure 6a as a function of the $[Fe_{Fe}^{\bullet}]$. Both $T_{Ea,set}$ and $T_{Ea,On}$ show a direct relation with hole concentration, as they decrease linearly as $[Fe_{Fe}^{\bullet}]$ rises. Moreover, a clear match in both trend and absolute value between T_N and $T_{Ea,On}$ is evident, which also includes the $T_{Ea,On}$ extracted from Xie et al. [18] and previously reported in Figure 3c. It is important to highlight that the $T_{Ea,On}$ and $T_{Ea,set}$ points from Xie et al. [18] and the T_N as a function of $[Fe_{Fe}^{\bullet}]$ relationship by Wattiaux et al.[53] were acquired using LSF samples with different Sr concentrations. In contrast, the measurements presented in this work have been performed using the same material while modifying $[Fe_{Fe}^{\bullet}]$ through adjustments of the oxygen vacancy

concentration. This emphasizes once again that the change of $[Fe_{Fe}^{\bullet}]$ in LSF50 is the true responsible for the change in the material properties.

The observed correspondence between T_{Ea} and T_N suggests a correlation between the magnetic order of the material and its activation energy. As the polaron hopping takes place through a Fe-O-Fe bond, the two main interactions play an important role in both electrical and magnetic response. Indeed, the elevated E_a associated with low $[Fe_{Fe}^{\bullet}]$ arises from spin restrictions inherent to SE interactions a mechanism also responsible for the AFM ordering. Hence, owing to spin constraints, hopping preferentially occurs within the nearest neighbor with the same spin orientation, leading to a hop to the second nearest neighbor (SNN) Fe site rather than the first (see AFM paths in **Figure 6b**). Indeed, DFT calculations on SNN hopping in LSF coincide with the experimental E_a=0.35eV measured in this work.[60] As expected for systems with competing DE and SE interactions, the increase of $[Fe_{Fe}^{\bullet}]$ leads to a weakening of the effective SE interaction, therefore lowering T_N.[51,52] When temperature reaches T_N, the thermal energy overcomes the preferential spin order and the hopping to the first nearest neighbor is favored (a process with a lower hopping energy, see PM in Figure 6b). This hypothesis also agrees with the shift in the A-transition energy, see Figure 6b. Therefore, the alignment of T_N and T_{Ea} is not coincidental but rather the main reason for the E_a change observed. The magnetic transition also provides an explanation for conventional measurements carried out at elevated temperatures, where conductivity could be readily explained by the polaron hopping model, with an E_a around 0.1 eV.[55] Since these measurements were performed at temperatures exceeding 500 ºC, LSF50 was always in its PM state, thus precluding the observation of spin ordering effects. Moreover, the exponential increase of σ_o with $[Fe_{Fe}^{\bullet}]$ is then restricted and particular of the AFM state. We also assign the origin of this exponential increase in conductivity with $[Fe_{Fe}^{\bullet}]$ to the SE-DE competition. It is well known that the increase of $[Fe_{Fe}^{\bullet}]$ increases the Fe 3d/O2p orbitals hybridization.[27,30] The increase in the delocalization of the polaron could lead to a higher hopping probability.[48] This explains why E_a maintains its value, as AFM order is preserved, but σ_o is exponentially affected by $[Fe_{Fe}^{\bullet}]$. Summarizing, our results demonstrate that the magnetic properties of LSF50 ruled by the concentration of $Fe_{Fe}^{\bullet}$ is at the origin of the modulation of its electrical properties.

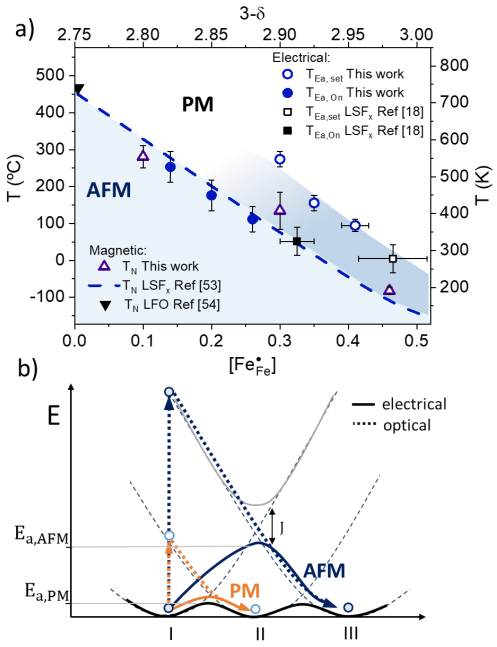

Figure 6 a) Magnetic phase diagram as a function of the concentration of holes. Electrical (T_{E_a}) and magnetic (T_N) transition temperatures in LSF50 are included. The figure shows the transitions from E_a=0.35eV ($T_{Ea,on}$) to an E_a=0.1eV ($T_{Ea,off}$), from both this study and Xie et al.[18] Neel Temperature (T_N) of LSF50 measured in this study and from Wattiaux et al.[53] and the one of LFO[54] are also included in the plot. **b)** Schematic representation of the origin of the change in E_a and $E_{a,opt}$. Blue paths show the case of an AFM ordering of the spins in the material, where the hopping to the neighboring site is not allowed. Orange paths show the classical interpretation of polaron transitions to adjacent sites.

2.6. Co-LSF50 exchange modulation through magnetoionic

The analog control of electrical, magnetic, and optical properties of LSF50 thin films could be used in the future in emerging fields, such as neuromorphic computing and magneto-ionics. To demonstrate a possible application of the AFM/PM transition taking place in LSF50 when modifying its oxidation state, in this section we have investigated how this effect can be used to manipulate AFM/FM exchange coupling in Co/LSF50 bilayers. It is known that ferromagnetic (FM) layers can be influenced by adjacent AFM films through interfacial exchange interactions. This phenomenon either induces a shift in the magnetic hysteresis loop (i.e., exchange bias, EB), or an increase of coercivity (H_C) when the FM spins are capable of dragging the AFM interfacial spins, through a microscopic exchange torque that leads to an extra energy cost for the overall magnetization reversal. This last situation is typically observed for loops of FM/AFM bilayers measured close to T_N.[61,62]

To study this effect, a new sample with 100 nm LSF50 was prepared following a procedure similar to the one proposed by Yildz et al. and, Huber et al. (see Experimental section).[63,64] The surface of the LSF50 film was proven (see Supplementary Material S1), and the roughness was below 2 nm uniformly along the film, therefore excluding stress effects contributing to the H_C variation. The sample allowed for an in-plane voltage application across two microfabricated gold rails forcing LSF50 to equilibrate at different oxidation states along the sample simultaneously from fully reduced to fully oxidized (see **Figure 7a**). A 2.5 nm Co layer and 2 nm Pt layer were sputtered on top of the LSF50 sample (see **Figure 7b**), and later studied by Magneto-Optical Kerr Effect (MOKE). In order to discard the possible effect coming from the potential CoO interlayer formation, XAS measurements on the Co L-edge were performed. The spectra for the Co seemed not to change along the stripe length and no Co oxidation was visible in the as-deposited (AD) sample (see Supplementary Material S10).

Hysteresis loops of the YSZ/LSF50/Co/Pt heterostructure were acquired at RT along the micro-fabricated rail, between the gold stripes using MOKE. **Figure 7c** shows the evolution of the hysteresis loops at X= 0, 0.75, 1.25 and 2.25 mm from the left contact of the rail. As can be seen, the AD Co loop in the reduced region (high T_N, left side of the figure) is less squared than in the oxidized region (low T_N, right side of the figure) and displays two contributions, with dissimilar coercivities. **Figure 7d** depicts the difference between the H_C of the Co on top of the LSF50 and the Co on top of the gold stripes, which should remain unbiased, along the stripe ($\Delta H_C = H_{C,LSF50} - H_{C,gold}$). Interestingly, a clear critical point is evident in the middle of the rail, where the coercivity of the Co on top of the LSF50 at the right side of such point increases with respect to the coercivity on top of the gold. After the substantial increase, a modest

decrease is also noticeable towards the rightmost area, but in no case the coercive field becomes the same as in the reduced part, which matches the coercivity values of the gold.

The sample was then subsequently field cooled (FC) at 50, 75, 100, 150, 200 and 250 ºC, with 10 kOe applied to try to induce EB. The evolution of the loops after each FC are shown in Figure 7c. Eventually, the soft contribution seen in the reduced states disappears as the FC temperature increases and no loop shift was seen in any of the measurements. A general decrease in H_C following each FC treatment was seen both in the Co located on top of the LSF50 and the gold. This phenomenon is ascribed to the loss of magnetic domains (and domain walls) in the Co layer, consequence of heating the sample and cooling it under a saturating field.[65] After the FC at 250 ºC the loops in the oxidized part are drastically modified, likely due to Co oxidizing from the LSF50 underneath. Figure 7d tracks the evolution of the coercivity after each FC treatment.

The critical point of the increase of H_C changed from X = 1.25 mm in the AD state to X = 1 mm after FC at 50 ºC, where the coercivity increases by 32 and 28.2 Oe compared to the Co on top of the gold stripes, respectively. After the FC at 200 ºC, H_C majorly decreases independently of the location in the rail, suggesting already partial Co oxidation. This was later confirmed performing the FC at 250 ºC, a process that modified not only the H_C but also the shape of the loops in the regions with more oxygen abundance (see Figure 7c).

The H_C trend observed in Figure 7d is consistent with the T_N observations from the previous sections. The Neel temperature is supposed to vary from 700 K to 100 K from the most reduced state to the most oxidized state. In the middle of the rail, T_N is presumably close to RT, allowing the FM Co spins to drag the interfacial AFM spins more easily, consequently increasing substantially H_C in that region. As *X* further increases, T_N decreases below RT and the material enters into the magnetic transition region. The FM layer remains pinned to the AFM. However, the Co requires less energy to drag the AFM spins, reducing the observed H_C. Therefore, an effect in the H_C was seen due to the exchange coupling between FM Co and the AFM LSFx underlayer. For lower X values, T_N is too high to have an impact on the FM layer as a field cooling overpassing its T_N would be needed. As we move towards higher X values, T_N eventually decreases and, consequently, the AFM interactions as well as the coupling with the FM become possible and then weaken when proceeding to increase X. Remarkably, if the annealing temperature is increased to attempt for an exchange bias in the lower X values zone, oxidation of the Co layer occurs before any effect is seen.

This high-throughput design with the thin Co on top promises avenues for implementation in devices. Especially considering that without thermal treatments, the AFM LSF50 with T_N close to RT already couples to the Co. Additionally, the possibility to tune magnetic and therefore, transport properties in an analog-like fashion, by gating with low voltages (<1 V), is appealing for memory devices and spintronics.

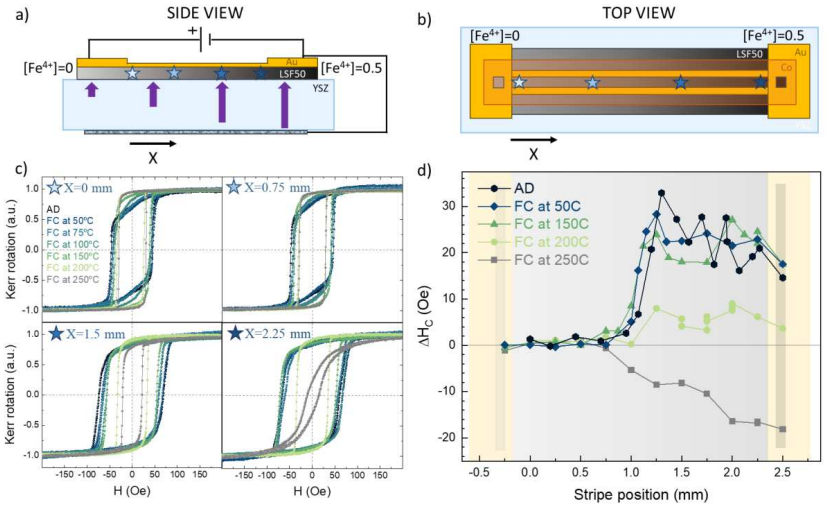

Figure 7 a) Schematic side view of the sample during the multi-state setting. b) Schematic top view of the sample after Co/Pt layer deposition. c) MOKE loops for the Co layer for 4 different positions along the rails measured in the as-deposited sample and after field cooling at different temperatures. d) Increase in coercivity of the Co loops after the different FC for the different positions along the rail compared to the Co deposited on top of the gold.

3. Conclusion

Fine-tuning of oxygen stoichiometry in mixed ionic-electronic conductive oxide of the $La_{1-x}Sr_xFeO_{3-\delta}$ family with x=0.5 was successfully achieved by applying small voltages through an electrochemical oxide-ion pump. Changes of several orders of magnitude in the polaronic conductivity were measured along oxygen deficiencies from δ=0 to 0.25 due to a variation of activation energy and pre-exponential factor. The origin of this electronic transition with temperature and point defect concentration was unveiled by simultaneously measuring of optical and magnetic properties. A close relation between the AFM/PM transition and the onset of the resistive state in LSFx was observed, with the T_N strongly dependent on $[Fe_{Fe}^{\bullet}]$. Due to this magnetic transition, the polaron hopping varies from second-nearest-neighbors in the AFM state to the nearest-neighbor in the PM phase above T_N, giving rise to a decrease of the polaronic activation energy and an increase of electronic conductivity. The modulation of the defect concentration achieved by electrochemical potential reported here opens the possibility of using voltage to control the functional properties of mixed ionic-electronic conductor (MIEC) materials in an analog manner, enabling their application in switching and modulation devices as well as for their performance optimization. Finally, benefiting from the voltage-controlled AFM/PM transition, a magneto-ionic control of the coercivity in a coupled FM Cobalt layer grown on top of a LSF50 layer with different oxygen content was demonstrated.

4. Experimental Section/Methods

Sample fabrication: LSF50 thin films were fabricated using Pulsed Laser Deposition (PLD) on gadolinium-doped ceria (CGO)-coated YSZ (001) 1x1cm^2 substrates. The protective CGO layer with a thickness of approximately 20 nm was deposited onto the YSZ substrates to prevent the formation of secondary phases at the interface with LSF with YSZ.[66,67] A commercial pellet of CGO was used as target material, while the pellet of LSF50 were prepared by solid state synthesis as explained in Tang et al, 2021.[36] All the layers were deposited employing a large-area system from PVD products (PLD-5000) equipped with a KrF-248 nm excimer laser from Lambda Physik (COMPex PRO 205). The films were grown with an energy fluency of 0.8 J cm^{-2} per pulse at a frequency of 10 Hz. The substrate was kept at 600 °C, in an oxygen partial pressure of 0.0067 mbar during the deposition and the substrate-target distance was set to 90 mm. Deposition conditions were chosen from previous optimization of the epitaxial growth of perovskites oxides to ensure a fully ordered and stoichiometric thin films, especially regarding the B/A ratio.[36,68,69] The deposition of the functional layer was done using a microfabricated Si mask with a size of 2.5x3.5mm^2 centered in the substrate. The thickness and roughness of the deposition were checked prior to the following fabrication steps allowing for a measurement of 99 nm thicknesses for LSF50 (see Supplementary Material Figure S1). To electrically contact the functional thin film, a conductive 10 nm Ti /100 nm Au electrode was microfabricated by photolithography and thermal evaporation. The thin Ti layer in the contact is deposited in order to enhance a good adhesion of the Au to the sample. To prevent the equilibrium of the functional layer with the atmosphere when going to higher temperatures, a last capping layer of alumina (Al_2O_3) of approximately 100 nm was also deposited via PLD (see a schematic of the samples in Figure 1a). Pressure, distance, frequency and energy parameters of the deposition were kept the same as for the previous layers, only the number of pulses was modified to adjust it to the desired thickness. Alumina was chosen as the capping material because of its low oxygen mobility and negligible oxygen stoichiometry variation in a wide range of oxygen partial pressure (pO_2) and temperatures. Another important property of the alumina capping is its low absorption, which allow to measure the optical properties of the functional layer with more precision. The Al_2O_3 did not cover the entire area of the sample area, allowing for a direct contact between the tips and the Au stripes close to the edges. Silver paste was also used on the backside of the YSZ substrate as counter electrode.

For the MOKE characterization of Co-LSF50 interaction, a different sample was used. In this case, 100 nm LSF50 deposited on 20 nm gadolinium-doped ceria (CGO)-coated Yttria Stabilized Zirconia (YSZ) (001) 0.5x0.5 cm^2 substrates was prepared. For this sample, 10 nm

Ti/100 nm Au with a design consisting in two pads connected by a pair of parallel stripes was used as working electrode (WE) (see sketch in Figure 7a and 7b). The separation between pads was 2.3mm and the stripes had 50 µm width and 100µm separation between them. One of the top pads was grounded with the silver painted in the bottom part serving as counter electrode (CE). This allowed for an in-plane voltage application that also forced the voltage difference between the WE and the CE. The linear potential drop in the layer allowed for the equilibration of the functional layer's oxidation state to different potentials all along the stripes' direction, i.e., allowing to have all the studied $[Fe_{Fe}^{\bullet}]$ in a single sample simultaneously (see Figure 7a). After the state was set at 350ºC applying a voltage difference between pads of -0.55V, the states were quenched by cooling down at 30ºC/min while keeping the voltage difference. Color gradient of the LSF50 in the stripe's direction was observed, confirming the multi-state presence. A 2.5 nm Co layer and 2 nm Pt layer were sputtered on top of the previously described microfabricated gold rails in order to study the imprint of the antiferromagnetic domains of LSF50 onto the Co layer.

Thin Film Characterization: Structural characterization and growth quality study of the as prepared sample was performed by XRD by using a lab diffractometer with 4-angle goniometer (MRD X'Pert Pro from Malvern-Panalytical) and Cu Kα tube and 2 × Ge(110) monochromator. These include Phi scans around 202 YSZ, 202 CGO, and the 101 of LSF50 peaks, respectivity; as well as pole figures around the at the LSF(111) reflection. For the cell parameter variation, X-ray diffraction patterns were also recorded using a Bruker D8 Advanced diffractometer with Cu Kα radiation (λ = 1.5406 Å) in a coupled Θ–2Θ Bragg–Brentano configuration. X'Pert PRO MPD analytical diffractometer (Panalytical) at 45 kV and 40 mA using CuKα radiation was also used for a deeper microstructural characterization and phase identification. The topography of the thin films and film thickness measurements were also assessed with an atomic force microscope XE 100 model from Park System Corp in non-contact mode.

Electrical and electrochemical characterization: Electrical conductivity measurements of the thin film were performed at different temperatures using a heating stage (Linkam instruments THMS600E-2) and 4-probe measurements with a Keithley 2400. Electrochemical characterization of the sample was also performed using a Biologic (model SP-150). A DC voltage bias from 0.1 V to −0.45 V was applied at different bias steps between the top gold contacts and the back-side Ag counter-electrode. Once the current was stabilized, the electrochemical impedance spectra (EIS) were recorded within a frequency range of 0.1 Hz-1MHz and an amplitude of 10mV. After the stabilization, electronic conductivity of the LSF

thin film was measured. In order to rule out the resistance of the contacts (e.g. from Ti interlayer oxidation), the film conductivity (σ) was measured using a 4-point probes method, considering the distance between the voltage sense connections (L=1.5mm), the width of the layer (d=3.5mm) and its thickness (t). Conductivity values were obtained through the relation between the electrical and geometrical parameters given by $R=I_R/V_R=L\cdot t^{-1}\cdot d^{-1}\cdot\sigma^{-1}$. All the experiments were carried out in atmospheric air.

Spectroscopic Ellipsometry Measurements: Spectroscopic ellipsometry, performed with the UVISEL ellipsometer from Horiba scientific, measured the optical constants of LSF thin films within a photon energy range from 0.6 to 5.0 eV with 0.05 eV intervals, using a 70° incident light beam. The data acquired from ellipsometry were subjected to modeling and fitting via Horiba Scientific's DeltaPsi2 software. In-situ ellipsometry measurements were carried out at different temperatures, following each voltage bias step.

Magnetization characterization: In-plane temperature vs Magnetization measurements were performed on a LakeShore 8600 series vibrating sample magnetometer (VSM) by means of an adjustable oven. The field was kept constant at 1kOe during the measurements. Cooled nitrogen (<350 K) and heated argon (>350 K) were injected in the oven to ensure thermal conductivity inside it. A NanoMOKE3 magnetooptical Kerr microscope was used to perform longitudinal MOKE measurements with a linearly polarized laser spot size of 3 μm and a wavelength of 660 nm. An in-plane variable magnetic field was applied along the gold stripes with a maximum value of ±400 Oe during the measurements, with a frequency of 7.3 Hz. To account for statistics at this high frequency, a minimum of 300 loops were always averaged before obtaining the shown loops.

PEEM imaging: X-ray photoemission-electron microscopy studies were carried out using the SPEEM end-station at UE49-PGMa beamline at the synchrotron radiation facility BESSY II operated by Helmholtz- Zentrum Berlin (HZB)[70]. The angle of incidence of the incoming X-ray radiation with respect to the sample surface was 16°. Magnetic imaging was always performed in zero external field. PEEM images were collected at 721.0 and 722.5 eV, at the Fe L_2-edge. A total of 80 images, each with a 3s integration time, were collected at each energy. Field of view was 10μm x 10μm, 514 x 514 pixels. Prior averaging the images, their drift was corrected. The XMLD images were obtained as (A –B)/(A + B), where A and B were the averaged images for each of the chosen energies, respectively. Due to the low XMLD signal, a modulation of the intensity caused by interferences of the incoming beam with the exit slit is

visible across the original images. This modulation was removed by subtracting to the XMLD image a twin image after applying a 50 x 50 averaged filter.

Supplementary Material

See the Supplementary Material for the surface and crystallographic characterization of the layers. Details on the sample performance and changes in optical properties of the functional film are discussed. In-deep conductivity changes are analyzed with different models and comparison with reference data for oxidized Sr-dopped lanthanum ferrites are also provided. Additionally, results from the magnetic characterization and X-ray absorption spectroscopy results are shown.

Acknowledgements

This project received funding from the European Union's Horizon 2020 research and innovation program under grant agreement No. 824072 (HARVESTORE), No 101066321 (TRANSIONICS) and, No. 101017709 (EPISTORE) and under the Marie Skłodowska-Curie grant agreement No 840787 (Thin-CATALYzER). F.C. acknowledges funding from a Marie Skłodowska Curie Actions Postdoctoral Fellowship grant (101107093). The authors acknowledge support from the Generalitat de Catalunya (2021-SGR-00750, NANOEN). Financial support from the European Research Council (2021-ERC-Advanced REMINDS Grant Nº 101054687), the Spanish Government (PID2020-116844RB-C21 and PID2021-127397NB-I00) and the Generalitat de Catalunya (2021-SGR-00651 and 2021SGR00328) is acknowledged. The authors acknowledge the support provided by the European Union FEDER funds. The authors also thank the Helmholtz-Zentrum Berlin for the provision of access to synchrotron radiation facilities and allocation of synchrotron radiation at SPEEM end-station of UE46-PGMa.

Author declarations section

The authors have no conflicts to disclose.

Data availability

The data that support the findings of this study are available from the corresponding author upon reasonable request.

References

[1] T. Defferriere, D. Klotz, J. Carlos Gonzalez-Rosillo, J.L. M Rupp, and H.L. Tuller, "Photo-enhanced ionic conductivity across grain boundaries in polycrystalline ceramics," Nature **21**, 438–444 (2022).
[2] F. Chiabrera, I. Garbayo, D. Pla, M. Burriel, F. Wilhelm, A. Rogalev, M. Núñez, A. Morata, and A. Tarancón, "Unraveling bulk and grain boundary electrical properties in La 0.8 Sr 0.2 Mn 1-y O 3± δ thin films," APL Mater **7**(013205), (2019).
[3] A. Urushibara, Y. Moritomo, T. Arima, A. Asamitsu, G. Kido, and Y. Tokura, "Insulator-metal transition and giant magnetoresistance in La1-xSrxMnO3," Phys Rev B **51**(20), 14103 (1995).
[4] L. Wang, R. Merkle, Y.A. Mastrikov, E.A. Kotomin, and J. Maier, "Oxygen exchange kinetics on solid oxide fuel cell cathode materials-general trends and their mechanistic interpretation," J Mater Res **27**(15), 2000–2008 (2012).
[5] J.T. Mefford, X. Rong, A.M. Abakumov, W.G. Hardin, S. Dai, A.M. Kolpak, K.P. Johnston, and K.J. Stevenson, "Water electrolysis on La1−xSrxCoO3−δ perovskite electrocatalysts," Nature Communications 2016 7:1 **7**(1), 1–11 (2016).
[6] Z. Shen, Y. Zhuang, W. Li, X. Huang, F.E. Oropeza, E.J.M. Hensen, J.P. Hofmann, M. Cui, A. Tadich, D. Qi, J. Cheng, J. Li, and K.H.L. Zhang, "Increased activity in the oxygen evolution reaction by Fe4+-induced hole states in perovskite La1−xSrxFeO3," J Mater Chem A Mater **8**(8), 4407–4415 (2020).
[7] L. Wang, Z. Yang, M.E. Bowden, and Y. Du, "Brownmillerite phase formation and evolution in epitaxial strontium ferrite heterostructures," Appl Phys Lett **114**(23), (2019).
[8] R. Von Helmolt, J. Wecker, B. Holzapfel, L. Schultz, and K. Samwer, "Giant negative magnetoresistance in perovskitelike La2/3Ba1/3MnOx ferromagnetic films," Phys Rev Lett **71**(14), 2331 (1993).
[9] S. Jana, S.K. Panda, D. Phuyal, B. Pal, S. Mukherjee, A. Dutta, P.A. Kumar, D. Hedlund, J. Schött, P. Thunström, Y. Kvashnin, H. Rensmo, M.V. Kamalakar, C.U. Segre, P. Svedlindh, K. Gunnarsson, S. Biermann, O. Eriksson, O. Karis, and D.D. Sarma, "Charge disproportionate antiferromagnetism at the verge of the insulator-metal transition in doped LaFeO3," Phys Rev B **99**(7), 075106 (2019).
[10] C.N.R. Rao, P. Ganguly, K. Sreedhar, R.A. Mohan Ram, and P.R. Sarode, "High-temperature superconductivity in YBa2Cu3O7 and related perovskite oxides: Some aspects of solid state chemistry," Mater Res Bull **22**(6), 849–855 (1987).
[11] A. Sood, A.D. Poletayev, D.A. Cogswell, P.M. Csernica, J.T. Mefford, D. Fraggedakis, M.F. Toney, A.M. Lindenberg, M.Z. Bazant, and W.C. Chueh, "Electrochemical ion insertion from the atomic to the device scale," Nature Reviews Materials 2021 6:9 **6**(9), 847–867 (2021).
[12] F. Chiabrera, I. Garbayo, L. López-Conesa, G. Martín, A. Ruiz-Caridad, M. Walls, L. Ruiz-González, A. Kordatos, M. Núñez, A. Morata, S. Estradé, A. Chroneos, F. Peiró, A. Tarancón, F. Chiabrera, I. Garbayo, M. Núñez, A. Morata, A. Tarancón, L. López-Conesa, G. Martín, A. Ruiz-Caridad, S. Estradé, F. Peiró, M. Walls, L. Ruiz-González, A. Kordatos, and A. Chroneos, "Engineering Transport in Manganites by Tuning Local Nonstoichiometry in Grain Boundaries," Advanced Materials **31**(4), 1805360 (2019).
[13] M. Coll, J. Fontcuberta, M. Althammer, M. Bibes, H. Boschker, A. Calleja, G. Cheng, M. Cuoco, R. Dittmann, B. Dkhil, I. El Baggari, M. Fanciulli, I. Fina, E. Fortunato, C. Frontera, S. Fujita, V. Garcia, S.T.B. Goennenwein, C.G. Granqvist, J. Grollier, R. Gross, A. Hagfeldt, G. Herranz, K. Hono, E. Houwman, M. Huijben, A. Kalaboukhov, D.J. Keeble, G. Koster, L.F. Kourkoutis, J. Levy, M. Lira-Cantu, J.L. MacManus-Driscoll, J. Mannhart, R. Martins, S. Menzel, T. Mikolajick, M. Napari, M.D. Nguyen, G. Niklasson, C. Paillard, S. Panigrahi, G. Rijnders, F. Sánchez, P. Sanchis, S. Sanna, D.G. Schlom, U. Schroeder, K.M. Shen, A.

Siemon, M. Spreitzer, H. Sukegawa, R. Tamayo, J. van den Brink, N. Pryds, and F.M. Granozio, "Towards Oxide Electronics: a Roadmap," Appl Surf Sci **482**, 1–93 (2019).
[14] D.S. Kim, V.J. Watkins, L.A. Cline, J. Li, K. Sun, J.D. Sugar, E.J. Fuller, A.A. Talin, Y. Li, D.S. Kim, V.J. Watkins, L.A. Cline, J. Li, K. Sun, Y. Li, J.D. Sugar, E.J. Fuller, and A.A. Talin, "Nonvolatile Electrochemical Random-Access Memory under Short Circuit," Adv Electron Mater **9**(1), 2200958 (2023).
[15] S.P. Simner, J.F. Bonnett, N.L. Canfield, K.D. Meinhardt, V.L. Sprenkle, and J.W. Stevenson, "Optimized lanthanum ferrite-based cathodes for anode-supported SOFCs," Electrochemical and Solid-State Letters **5**(7), A173 (2002).
[16] R.P. Forslund, W.G. Hardin, X. Rong, A.M. Abakumov, D. Filimonov, C.T. Alexander, J.T. Mefford, H. Iyer, A.M. Kolpak, K.P. Johnston, and K.J. Stevenson, "Exceptional electrocatalytic oxygen evolution via tunable charge transfer interactions in La0.5Sr1.5Ni1−xFexO4±δ Ruddlesden-Popper oxides," Nature Communications 2018 9:1 **9**(1), 1–11 (2018).
[17] A.L. Krick, and S.J. May, "Evidence for oxygen vacancy manipulation in La1/3Sr2/3FeO3−δ thin films via voltage controlled solid-state ionic gating," APL Mater **5**(4), 42504 (2017).
[18] Y.J. Xie, M.D. Scafetta, E.J. Moon, A.L. Krick, R.J. Sichel-Tissot, and S.J. May, "Electronic phase diagram of epitaxial La1-xSr xFeO3 films," Appl Phys Lett **105**(6), 62110 (2014).
[19] Y. Xie, M.D. Scafetta, R.J. Sichel-Tissot, E. Ju Moon, R.C. Devlin, H. Wu, A.L. Krick, S.J. May, Y.J. Xie, M.D. Scafetta, R.J. Sichel-Tissot, E.J. Moon, R.C. Devlin, H. Wu, A. Krick, and S.J. May, "Control of Functional Responses Via Reversible Oxygen Loss in La 1-x Sr x FeO 3-δ Films," Advanced Materials **26**, 1434–1438 (2014).
[20] M. V. Patrakeev, J.A. Bahteeva, E.B. Mitberg, I.A. Leonidov, V.L. Kozhevnikov, and K.R. Poeppelmeier, "Electron/hole and ion transport in La1−xSrxFeO3−δ," J Solid State Chem **172**(1), 219–231 (2003).
[21] I.A. Leonidov, V.L. Kozhevnikov, M. V. Patrakeev, E.B. Mitberg, and K.R. Poeppelmeier, "High-temperature electrical conductivity of Sr0.7La0.3FeO3−δ," Solid State Ion **144**(3–4), 361–369 (2001).
[22] Z. Bian, Q. Yang, M. Yoshimura, H.J. Cho, J. Lee, H. Jeen, T. Endo, Y. Matsuo, and H. Ohta, "Solid-State Electrochemical Thermal Transistors with Strontium Cobaltite-Strontium Ferrite Solid Solutions as the Active Layers," ACS Appl Mater Interfaces **15**(19), 23512–23517 (2023).
[23] S. He, O. Petracic, V. Lauter, L. Cao, Y. Zhou, M.L. Weber, J. Schubert, O. Concepción, R. Dittmann, R. Waser, T. Brückel, and F. Gunkel, "La0.6Sr0.4CoO3−δ Films Under Deoxygenation: Magnetic And Electronic Transitions Are Apart from The Structural Phase Transition," Adv Funct Mater **34**(24), 2313208 (2024).
[24] J. Mizusaki, M. Yoshihiro, S. Yamauchi, and K. Fueki, "Nonstoichiometry and defect structure of the perovskite-type oxides La1−xSrxFeO3−°," J Solid State Chem **58**(2), 257–266 (1985).
[25] M. V. Patrakeev, I.A. Leonidov, V.L. Kozhevnikov, and K.R. Poeppelmeier, "p-Type electron transport in La1−xSrxFeO3−δ at high temperatures," J Solid State Chem **178**(3), 921–927 (2005).
[26] J. Mizusaki, T. Sasamoto, W.R. Cannon, and H.K. Bowen, "Electronic Conductivity, Seebeck Coefficient, and Defect Structure of LaFeO3," Journal of the American Ceramic Society **65**(8), 363–368 (1982).
[27] L. Wang, Y. Du, P. V. Sushko, M.E. Bowden, K.A. Stoerzinger, S.M. Heald, M.D. Scafetta, T.C. Kaspar, and S.A. Chambers, "Hole-induced electronic and optical transitions in L a1-x S rxFe O3 epitaxial thin films," Phys Rev Mater **3**(2), 025401 (2019).

[28] W.H. Jung, and E. Iguchi, "Polaronic transport properties in La1-xSrxFeO3 systems (0.05<or=x<or=0.3)," Journal of Physics: Condensed Matter **7**(6), 1215 (1995).
[29] M. Søgaard, P. Vang Hendriksen, and M. Mogensen, "Oxygen nonstoichiometry and transport properties of strontium substituted lanthanum ferrite," J Solid State Chem **180**(4), 1489–1503 (2007).
[30] Y. Shin, K.Y. Doh, S.H. Kim, J.H. Lee, H. Bae, S.J. Song, and D. Lee, "Effect of oxygen vacancies on electrical conductivity of La0.5Sr0.5FeO3−δ from first-principles calculations," J Mater Chem A Mater **8**(9), 4784–4789 (2020).
[31] J.K. Wenderott, E.M. Dufresne, Y. Li, H. Cao, Q. Zhang, K.V.L. V Narayanachari, D. Bruce Buchholz, S. Guha, D.D. Fong, J.K. Wenderott, Y. Li, H. Cao, S. Guha, D.D. Fong, E.M. Dufresne, Q. Zhang, and D.B. Buchholz, "The Dynamics of Oxygen Ion Exchange in Epitaxial Strontium Cobaltite Bilayers," Adv Mater Interfaces **10**(21), 2300127 (2023).
[32] Q. Zhang, G. Hu, V. Starchenko, G. Wan, E.M. Dufresne, Y. Dong, H. Liu, H. Zhou, H. Jeen, K. Saritas, J.T. Krogel, F.A. Reboredo, H.N. Lee, A.R. Sandy, I.C. Almazan, P. Ganesh, and D.D. Fong, "Phase Transition Dynamics in a Complex Oxide Heterostructure," Phys Rev Lett **129**(23), 235701 (2022).
[33] A. Braun, J. Richter, A.S. Harvey, S. Erat, A. Infortuna, A. Frei, E. Pomjakushina, B.S. Mun, P. Holtappels, U. Vogt, K. Conder, L.J. Gauckler, and T. Graule, "Electron hole-phonon interaction, correlation of structure, and conductivity in single crystal La0.9Sr0.1FeO 3-δ," Appl Phys Lett **93**(26), (2008).
[34] T. Katase, Y. Suzuki, and H. Ohta, "Reversibly Switchable Electromagnetic Device with Leakage-Free Electrolyte," Adv Electron Mater **2**(6), 1600044 (2016).
[35] C.S. Kim, K.W. Park, and H.L. Tuller, "Electrochemically controlled defect chemistry: From oxygen excess to deficiency," Acta Mater **211**, 116866 (2021).
[36] Y. Tang, F. Chiabrera, A. Morata, I. Garbayo, N. Alayo, A. Tarancón, Y. Tang, F. Chiabrera, A. Morata, I. Garbayo, N. Alayo, and A. Tarancón, "Pushing the Study of Point Defects in Thin Film Ferrites to Low Temperatures Using In Situ Ellipsometry," Adv Mater Interfaces **8**(6), 2001881 (2021).
[37] A. Schmid, G.M. Rupp, and J. Fleig, "Voltage and partial pressure dependent defect chemistry in (La,Sr)FeO 3−δ thin films investigated by chemical capacitance measurements," Physical Chemistry Chemical Physics **20**(17), 12016–12026 (2018).
[38] A. Schmid, M. Krammer, and J. Fleig, "Rechargeable Oxide Ion Batteries Based on Mixed Conducting Oxide Electrodes," Adv Energy Mater **13**(11), 2203789 (2023).
[39] D. Chen, S.R. Bishop, and H.L. Tuller, "Non-stoichiometry in Oxide Thin Films: A Chemical Capacitance Study of the Praseodymium-Cerium Oxide System," Adv Funct Mater **23**(17), 2168–2174 (2013).
[40] D. Marrocchelli, S.R. Bishop, H.L. Tuller, and B. Yildiz, "Understanding Chemical Expansion in Non-Stoichiometric Oxides: Ceria and Zirconia Case Studies," Adv Funct Mater **22**(9), 1958–1965 (2012).
[41] C. Chatzichristodoulou, P. Norby, P. V. Hendriksen, and M.B. Mogensen, "Size of oxide vacancies in fluorite and perovskite structured oxides," J Electroceram **34**(1), 100–107 (2015).
[42] O. Clemens, M. Kuhn, and R. Haberkorn, "Synthesis and characterization of the La1−xSrxFeO3−δ system and the fluorinated phases La1−xSrxFeO3−xFx," J Solid State Chem **184**(11), 2870–2876 (2011).
[43] M.D. Scafetta, Y.J. Xie, M. Torres, J.E. Spanier, and S.J. May, "Optical absorption in epitaxial La1-xSrx FeO 3 thin films," Appl Phys Lett **102**(8), (2013).
[44] D. Worledge, L. Miéville, and T. Geballe, "On-site Coulomb repulsion in the small polaron system La1-xCacMnO3," Phys Rev B **57**(24), 15267 (1998).
[45] D. Emin, and T. Holstein, "Studies of small-polaron motion IV. Adiabatic theory of the Hall effect," Ann Phys (N Y) **53**(3), 439–520 (1969).

[46] J. Wang, K. Syed, S. Ning, I. Waluyo, A. Hunt, E.J. Crumlin, A.K. Opitz, C.A. Ross, W.J. Bowman, and B. Yildiz, "Exsolution Synthesis of Nanocomposite Perovskites with Tunable Electrical and Magnetic Properties," Adv Funct Mater **32**(9), 2108005 (2022).
[47] T. Maeder, and J.G. Bednorz, "Influence of oxygen stoichiometry on electrical transport and magnetic properties of doped perovskite-type ferrate and manganate single crystals," J Eur Ceram Soc **19**(6–7), 1507–1510 (1999).
[48] I.G. Austin, and N.F. Mott, "Polarons in crystalline and non-crystalline materials," Adv Phys **18**(71), 41–102 (1969).
[49] S. Mildner, J. Hoffmann, P.E. Blöchl, S. Techert, and C. Jooss, "Temperature- and doping-dependent optical absorption in the small-polaron system Pr1-xCaxMnO3," Phys Rev B Condens Matter Mater Phys **92**(3), 035145 (2015).
[50] J.B. Goodenough, "An interpretation of the magnetic properties of the perovskite-type mixed crystals La1−xSrxCoO3−λ," Journal of Physics and Chemistry of Solids **6**(2–3), 287–297 (1958).
[51] D. Golosov, and M. Norman, "Some aspects of the theory of magnets with competing double exchange and superexchange interactions," Phys Rev B **58**(13), 8617 (1998).
[52] P.G. De Gennes, "Effects of Double Exchange in Magnetic Crystals," Physical Review **118**(1), 141 (1960).
[53] A. Wattiaux, J.C. Grenier, M. Pouchard, and P. Hagenmuller, "Electrolytic Oxygen Evolution in Alkaline Medium on La1-xSrxFeO3 −y Perovskite-Related Ferrites: I . Electrochemical Study," J Electrochem Soc **134**(7), 1714–1718 (1987).
[54] J.W. Seo, E.E. Fullerton, F. Nolting, A. Scholl, J. Fompeyrine, and J.P. Locquet, "Antiferromagnetic LaFeO3 thin films and their effect on exchange bias," Journal of Physics Condensed Matter **20**(26), (2008).
[55] M. Onose, H. Takahashi, H. Sagayama, Y. Yamasaki, and S. Ishiwata, "Complete phase diagram of Sr1-xLaxFe O3 with versatile magnetic and charge ordering," Phys Rev Mater **4**(11), 114420 (2020).
[56] I. Hallsteinsen, A. Grutter, M. Moreau, S.D. Slöetjes, K. Kjærnes, E. Arenholz, and T. Tybell, "Role of antiferromagnetic spin axis on magnetic reconstructions at the (111)-oriented L a0.7Sr0.3MnO3/LaFe O3 interface," Phys Rev Mater **2**(8), (2018).
[57] A. Scholl, J. Stöhr, J. Lüning, J.W. Seo, J. Fompeyrine, H. Siegwart, J.P. Locquet, F. Nolting, S. Anders, E.E. Fullerton, M.R. Scheinfein, and H.A. Padmore, "Observation of antiferromagnetic domains in epitaxial thin films," Science (1979) **287**(5455), 1014–1016 (2000).
[58] F. Nolting, A. Scholl, J. Stöhr, J.W. Seo, J. Fompeyrine, H. Siegwart, J.P. Locquet, S. Anders, J. Lüning, E.E. Fullerton, M.F. Toney, M.R. Scheinfein, and H.A. Padmore, "Direct observation of the alignment of ferromagnetic spins by antiferromagnetic spins," Nature 2000 405:6788 **405**(6788), 767–769 (2000).
[59] E. Folven, Y. Takamura, and J.K. Grepstad, "X-PEEM study of antiferromagnetic domain patterns in LaFeO3 thin films and embedded nanostructures," J Electron Spectros Relat Phenomena **185**(10), 381–388 (2012).
[60] C. Hartmann, J. Laurencin, and G. Geneste, "Hole polarons in LaFeO3 and La1-xSrxFeO3-δ: Stability, trapping, mobility, effect of Sr concentration, and oxygen vacancies," Phys Rev B **107**(2), 024104 (2023).
[61] J. Nogués, and I.K. Schuller, "Exchange bias," J Magn Magn Mater **192**(2), 203–232 (1999).
[62] J. Nogués, J. Sort, V. Langlais, V. Skumryev, S. Suriñach, J.S. Muñoz, and M.D. Baró, "Exchange bias in nanostructures," Phys Rep **422**(3), 65–117 (2005).
[63] D. Kim, R. Bliem, F. Hess, J.J. Gallet, and B. Yildiz, "Electrochemical Polarization Dependence of the Elastic and Electrostatic Driving Forces to Aliovalent Dopant Segregation on LaMnO3," J Am Chem Soc **142**(7), 3548–3563 (2020).

[64] T.M. Huber, E. Navickas, K. Sasaki, B. Yildiz, H. Tuller, G. Friedbacher, H. Hutter, and J. Fleig, "Experimental Design for Voltage Driven Tracer Incorporation and Diffusion Studies on Oxide Thin Film Electrodes," J Electrochem Soc **164**(7), F809–F814 (2017).
[65] J.D. Livingston, "A review of coercivity mechanisms," J Appl Phys **52**(3), 2544–2548 (1981).
[66] S.P. Simner, J.P. Shelton, M.D. Anderson, and J.W. Stevenson, "Interaction between La(Sr)FeO3 SOFC cathode and YSZ electrolyte," Solid State Ion **161**(1–2), 11–18 (2003).
[67] D. Tian, B. Lin, Y. Yang, Y. Chen, X. Lu, Z. Wang, W. Liu, and E. Traversa, "Enhanced performance of symmetrical solid oxide fuel cells using a doped ceria buffer layer," Electrochim Acta **208**, 318–324 (2016).
[68] Y. Tang, F. Chiabrera, A. Morata, A. Cavallaro, M.O. Liedke, H. Avireddy, M. Maller, M. Butterling, A. Wagner, M. Stchakovsky, F. Baiutti, A. Aguadero, and A. Tarancón, "Ion Intercalation in Lanthanum Strontium Ferrite for Aqueous Electrochemical Energy Storage Devices," ACS Appl Mater Interfaces **14**(16), 18486–18497 (2022).
[69] F.M. Chiabrera, F. Baiutti, J.M. Börgers, G.F. Harrington, L. Yedra, M.O. Liedke, J. Kler, P. Nandi, J. de Dios Sirvent, J. Santiso, M. López-Haro, J.J. Calvino, S. Estradé, M. Butterling, A. Wagner, F. Peiró, R.A. De Souza, and A. Tarancón, "The impact of Mn nonstoichiometry on the oxygen mass transport properties of La0.8Sr0.2Mn y O3±δ thin films," JPhys Energy **4**(4), (2022).
[70] F. Kronast, and S.V. Molina, "SPEEM: The photoemission microscope at the dedicated microfocus PGM beamline UE49-PGMa at BESSY II," Journal of Large-Scale Research Facilities JLSRF **2**, A90–A90 (2016).